



Integrated Lagrangian and Eulerian 3D microstructure-explicit simulations for predicting macroscopic probabilistic SDT thresholds of energetic materials

Yaochi Wei¹ · Reetesh Ranjan² · Ushasi Roy¹ · Ju Hwan Shin¹ · Suresh Menon² · Min Zhou¹

Received: 8 February 2019 / Accepted: 19 May 2019 / Published online: 5 June 2019
© Springer-Verlag GmbH Germany, part of Springer Nature 2019

Abstract

Computational predictions of measures for macroscopic material attributes from the microstructure scale is a fundamental challenge in materials science. Data transfer across scales and physics-based models plays a central role in this highly material-specific process. Here, we present an approach for computationally establishing the probabilistic shock-to-detonation transition (SDT) threshold or “pop plot” (PP, the relation between run-to-detonation distance and applied pressure) of polymer-bonded explosives (PBXs) from three-dimensional (3D) simulations. The approach takes respective advantages of multiphysics Lagrangian and Eulerian modeling frameworks. The combined Lagrangian and Eulerian simulations provide an explicit account of 3D heterogeneous material microstructure at sizes up to tens of mm, mechanisms for the development of hotspots, and the coupled mechanical-thermal-chemical-transport processes which underlie the behaviors being predicted. Data transfers in the form of hotspot intensity fields from the Lagrangian simulations to the Eulerian simulations link the two frameworks. To capture the fundamental nature of the multiphysics processes, the source, and the propagation of the stochastic variations in material behavior, a 3D statistically equivalent microstructure sample set (SEMSS) is designed and used. The approach facilitates an efficient quantification of the probabilistic macroscopic detonation thresholds, leading to an analytical expression for the PP that accounts for both the microstructure effects and uncertainties. The material system modeled tracks the properties of PBX 9501 and the loading conditions studied involve shock pressure P_s in the range of 11–15 GPa. The results are in good agreement with available experimental data.

Keywords 3D microstructure · Shock to detonation · Energetic materials · Pop plot

1 Introduction

The class of energetic materials known as high explosives (HE) are primarily composites of organic energetic crystals and polymeric binders, although other components such as metal fuel granules and inorganic oxidizer particles can also be added. These materials are commonly referred to as polymer-bonded explosives or PBXs. The constituents and microstructure hierarchy from the atomistic, micro, meso, to macro scales determine ignition, shock-to-detonation tran-

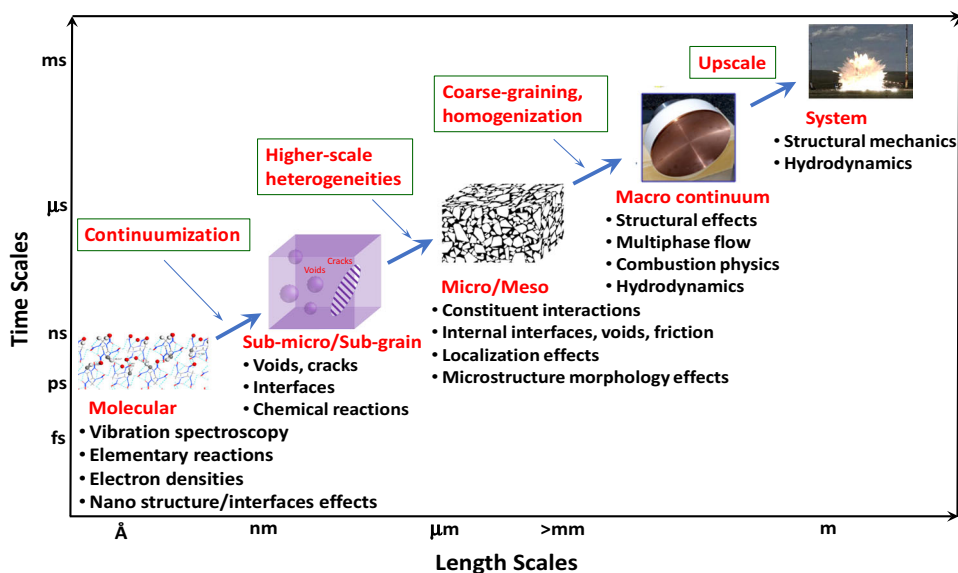
sition (SDT), and energy release (Fig. 1) [1]. The relevant physical and chemical processes require appropriate resolutions for responses at the different spatial and temporal scales. Different models are used at the requisite scales of interest. For example, atomistic models and reaction kinetics models are used at the nanoscale [2]; sub-micro (sub-grain) continuum models accounting for individual or clusters of defects (i.e., voids/cracks/interfaces) are used at the scale of microns to tens of microns (μm) [3–6]; microstructure-explicit models (MEM) are used at the micro-to-mm scales [1, 7]; and macro continuum models (homogenized) in hydrodynamic codes are used at the cm-to-m structure scales [8–11]. The finer-scale models provide input for the coarser-scale models. Sub-micro models for individual voids or a population of voids [6, 12, 13] focus on the effects of such geometric discontinuities that exist within individual constituents in a microstructure (Fig. 1). Such models do not concern the effects of heterogeneous material microstructures which

✉ Min Zhou
min.zhou@gatech.edu

¹ The George W. Woodruff School of Mechanical Engineering, School of Materials Science and Engineering, Georgia Institute of Technology, Atlanta, GA 30332-0405, USA

² School of Aerospace Engineering, Georgia Institute of Technology, Atlanta, GA 30332-0150, USA

Fig. 1 Multiscale nature of structure, performance, and models of energetic materials and influences across the scales



have constituent size scales (e.g., grain size) on the order of tens to hundreds of microns [14]. The microstructure (sometimes also referred to as the meso) scale concerns material heterogeneities (grains, binder, metal fuel granules, and inorganic oxidizer particles) on the order of tens to hundreds of microns. It is at this scale that processing and synthesis have the most influence on structure and properties. Also at this scale the sub-micro scale, hotspots from heterogeneous constituent inelasticity, void collapse, and crack/interface sliding manifest and influence the ignition, reaction, and detonation of the materials. To reach the macroscale “from the ground up”, it is necessary to fully account for the heterogeneous material microstructure. As a result, characterization and model development at this scale are a primary focus of material design and engineering. Because the size scale of the constituents is on the order of hundreds of microns [14, 15], sufficiently representative samples must be of the order of mm or tens of mm [7]. As far as we know so far, with the exception of [16, 17], most such microstructure-explicit models (MEM) in this regard are two-dimensional (2D) plane-strain models [1, 3, 18]. These models can be regarded as based on sections of the true three-dimensional (3D) microstructures.

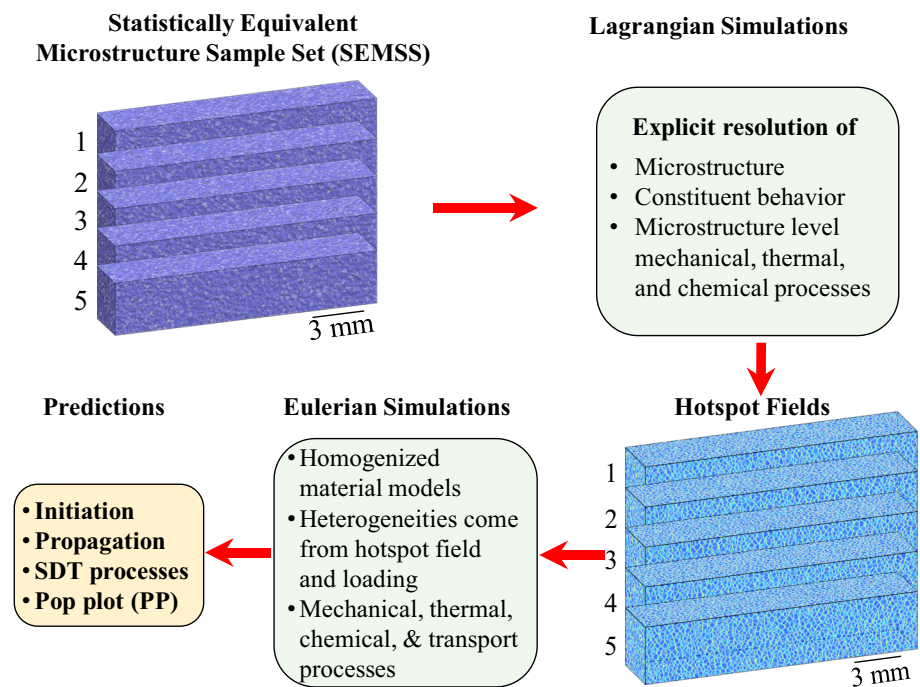
Heterogeneities such as constituent variations, interfaces, voids, cracks, and variability in material processing (e.g., batch variations) are important sources of uncertainty or stochastic variations in behaviors at different scales. The lack of consideration for microstructure and uncertainties limits the usefulness of macroscopic models in (a) linking the design, development, and selection of intentionally structured energetic materials (EM) to real macroscopic performance (b) transitioning macroscopic analyses from empiricism to predictive science for real materials and structures, and (c) quantifying the ranges of EM performance,

components and systems with regard to precision, reliability, and margin of safety. As a result, there is a need to account for both the microstructure effects and stochastic variations in macroscopic energetic behaviors of the materials.

Significant advances have been made in microstructure-explicit models and computational platforms that use Lagrangian (L), Eulerian (E), or mixed L/E approaches [1, 4, 7, 8, 19] which have different focuses. Lagrangian approaches [1, 7] have the advantage of being able to readily and explicitly track constituents, fracture, friction, and frictional heating, but are less suited for resolving voids and extremely severe deformations of transition from condensed phases to gas phases. As a result, they are more appropriate for processes leading up to and around the initiation of chemical reaction in energetic materials. Eulerian approaches [3, 4, 8, 20], on the other hand, have the advantages of being able to explicitly track void collapse, severe flow, jetting, and SDT, but are less capable of resolving and tracking evolution of heterogeneous microstructures, fracture, friction, and frictional heating. Consequently, they are more extensively used for reactions, transition from shock loading to detonation, and reactive flow. Although arbitrary Lagrangian and Eulerian (ALE) codes are available [5, 10, 19, 21, 22], they are extremely computationally expensive, have so far not been used for highly heterogeneous materials, and are only practical for problems at size scales of microns or tens of microns at most [5, 21, 23].

Here in this paper, we combine Lagrangian and Eulerian approaches for coordinated three-dimensional (3D) microstructure-explicit simulations (MES) to predict the reaction initiation, reaction propagation, and *probabilistic macroscopic pop plot* (PP) of PBXs. The framework is illustrated in Fig. 2. The characteristic microstructure size scale (grain size) is on the order of hundreds of microns. The

Fig. 2 Framework for integrated Lagrangian and Eulerian simulations for predicting the reaction initiation, reaction propagation, and probabilistic pop plot (PP) of heterogeneous energetic materials



3D models are 15 mm \times 3 mm \times 3 mm in size, providing sufficient representation of the material microstructure and allowing the analyses to reach the macroscale. The Lagrangian part focuses on resolving the microstructure effects and heating due to the microstructure effects. The Eulerian part focuses on the initiation and propagation of reaction, the SDT process, and the characterization of the PP. The two parts are linked via a hotspot field determined from the Lagrangian part which embodies the microstructure effects on dissipation and heating that are responsible for triggering the heterogeneous ignition and detonation process. To account for the stochastic variations in material behavior due to variations at the microstructure level, a statistically equivalent microstructure sample set (SEMSS) with prescribed statistical microstructure attributes consistent with those of PBX 9501 is generated and used. The use of the SEMSS allows probabilistic pop plots to be obtained. The approach used here lends itself to uncertainty quantification (UQ) [24–30] to characterize the variations in the macroscopic behavior due to variations in material parameters. In the analysis carried out there, the SEMSS allows the *probabilistic* SDT threshold and an analytical expression for the SDT threshold (pop plot or PP) to be developed for the first time as far as the authors are aware.

This paper is organized as follows. Section 2 describes the material analyzed and the integrated Lagrangian and Eulerian computational framework. Section 3 discusses the simulated SDT process and the predicted pop plots. A particular emphasis is placed on quantifying the probabilistic nature of SDT resulting from intrinsic material heterogeneities.

2 Framework of analysis

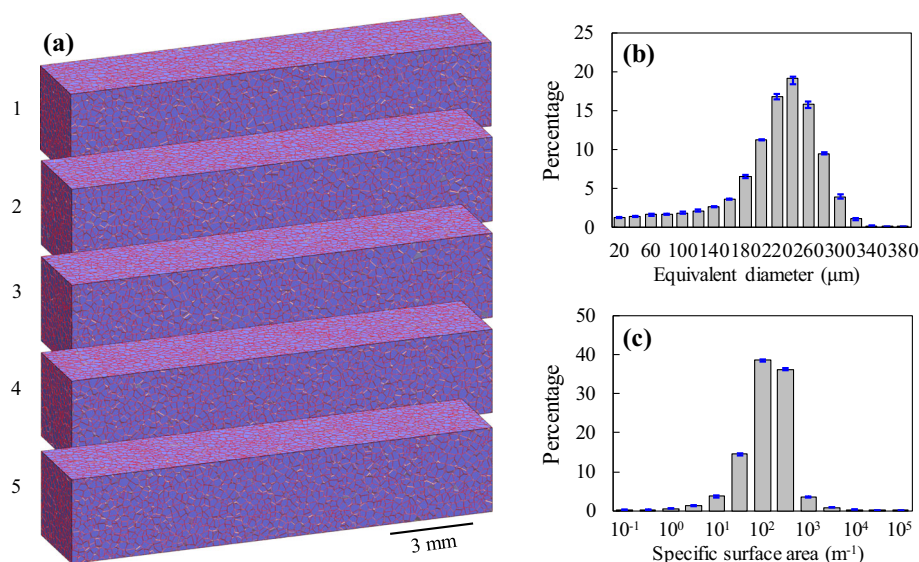
In this section, first, a brief description of the energetic materials and underlying micro-structures is presented. Subsequently, sub-models corresponding to the Lagrangian and Eulerian simulations and the coupling between the simulations are discussed. The computational setup for the SDT study is also described.

2.1 Material and microstructures

Polymer-bonded explosives (PBXs) considered here are heterogeneous composites consisting of energetic particles and a polymer binder. The energetic particles in practical use include HMX, RDX, TATB, and PETN. Among these, HMX (Octahydro-1,3,5,7-tetranitro-1,3,5,7-tetrazocine) holds the highest energy density, therefore, has drawn intense interest for several decades [23, 31–33]. HMX-based PBXs include PBX 9501, which consists of HMX (95 wt%), Estane (2.5 wt%), and a plasticizer (2.5 wt%).

In this study, the microstructures that are computationally generated have an HMX grain volume fraction of 81% and a binder volume fraction of 19%. The theoretical volume fraction of HMX in PBX 9501 is 92.7%. However, lower HMX volume fractions are observed in actual microstructures because some HMX particles are too small to be resolved and are absorbed in the binder, leading to what is sometimes referred to as the “dirty binder”. For example, Benson and Conley [34] observed a binder volume fraction of 26% (and grain volume fraction of 74%) from a micro-

Fig. 3 Computationally generated 3D statistically equivalent microstructure sample set (SEMSS) with a grain volume fraction of $\eta = 0.81$, **a** 3D images of five instantiations, **b** HMX grain size distributions, and **c** HMX grain-binder specific surface area distributions. The error bars indicate variations among the samples in the set



graph of PBX 9501 whose theoretical volume fraction of a binder is only around 8% (and grain volume fraction of 92%). Mas et al. [35] observed a binder volume fraction of 23% for PBX 9501 and reproduced the stress–strain behavior using an explicit finite element framework. Barua and Zhou [36] used the microstructures of PBX 9501 with a HMX volume fraction of 82% in their numerical study and obtained stress–strain curves that match experimental data. This paper uses the same HMX volume fraction for PBX microstructures and the same numerical framework (cohesive finite element method) as those used in [1]. Essentially in such analyses, the effects of the part of HMX absorbed in the binder and therefore not explicitly resolved can be considered as being lumped in the constitutive behavior of the binder. So far, there is a lack of more detailed study on the issue of the “dirty binder” [14, 34, 35].

The HMX particles in PBX microstructures typically have random polygonal shapes [34, 37, 38]. To obtain 3D PBX microstructures similar to those of experimental specimens, a library of HMX grains extracted from microstructures generated by 3D Voronoi tessellation is first established, with the sizes of the grains systematically tabulated. The grains are then used to compose PBX microstructures with prescribed grain volume fractions and grain size distributions. This approach allows large numbers of microstructure samples with prescribed grain size distributions and other attributes to be obtained efficiently. In this section and subsequent discussions, we use the term “samples” to indicate computationally generated microstructures for finite element simulations and “specimens” to indicate experimentally obtained microstructures. Five 3D samples with statistically equivalent attributes but different random distributions of the constituents are generated and used. Computationally analyzing the behavior of a statistically equivalent microstructure sample set (SEMSS)

via multiple simulations under the same conditions is the computational equivalent of carrying out experiments on multiple specimens of the same material, allowing the statistical variations and probabilistic distributions of material behavior to be quantified through multiple simulations on the SEMSS.

To illustrate the random variations in microstructure morphology and the statistical consistency among the multiple samples in the set, Fig. 3a shows five 3D samples with the same HMX volume fraction of $\eta = 0.81$ and Fig. 3b, c show the variations in grain size distributions and specific grain surface area (grain surface to grain volume ratio) distributions, respectively, among the samples. The grains have an average size of 207 μm and a monomodal size distribution with a standard deviation of 60.1 μm . The specific grain-binder interfaces (surface-to-volume ratios of grains) have an average of 184 m^{-1} .

2.2 The Lagrangian approach

In the Lagrangian approach, the stress tensor is decomposed into a hydrostatic part and a deviatoric part, i.e.,

$$\sigma_{ij} = -P\delta_{ij} + \sigma'_{ij}, \quad (1)$$

where σ_{ij} is the Cauchy stress and P is the negative of the hydrostatic stress (or pressure)

$$P = -\frac{1}{3}(\sigma_{11} + \sigma_{22} + \sigma_{33}) = -\frac{1}{3}\sigma_{ii}. \quad (2)$$

The hydrostatic part of the stress carried by all the constituents can be described by the Birch–Murnaghan or the

Mie–Grüneisen equations of state [39]. The Cauchy stress is related to the Kirchhoff stress via

$$\tau_{ij} = J\sigma_{ij}, \tag{3}$$

where $J = \det(\mathbf{F})$ is the Jacobian, with \mathbf{F} being the deformation gradient. The deviatoric constitutive behavior of the grains is described by

$$\hat{\boldsymbol{\tau}}' = \mathbf{L} : (\mathbf{D}' - \mathbf{D}'_p), \tag{4}$$

where \mathbf{L} is the tensor of elastic moduli and $\hat{\boldsymbol{\tau}}'$ is the deviatoric part of the Jaumann rate of the Kirchhoff stress. \mathbf{D}' in Eq. (4) is the deviatoric part of the rate of deformation \mathbf{D} , which can be decomposed into an elastic part and a viscoplastic part as

$$\mathbf{D}' = \mathbf{D}'_e + \mathbf{D}'_p. \tag{5}$$

In the above relation, \mathbf{D}'_p is the viscoplastic part of \mathbf{D}' in the form of

$$\mathbf{D}'_p = \frac{3\dot{\bar{\epsilon}}}{2\bar{\sigma}} \boldsymbol{\tau}', \text{ with } \bar{\sigma}^2 = \frac{3}{2} \boldsymbol{\tau}' : \boldsymbol{\tau}'. \tag{6}$$

Here, $\bar{\sigma}$ is the Misses equivalent stress, $\boldsymbol{\tau}'$ is the deviatoric part of the Kirchhoff stress, and $\dot{\bar{\epsilon}}$ is the temperature-dependent equivalent plastic strain rate which has the form as in Zhou et al. [40]. The parameters in the viscoplasticity model for HMX are listed in Table 2 in [1].

The binder in PBX 9501 is Estane. It follows the Generalized Maxwell Model (GMM) [41] in the form of

$$\boldsymbol{\sigma}(\tau) = \int_0^\tau 2G(t-t') \frac{\partial \boldsymbol{\epsilon}^D}{\partial t'} dt' + \int_0^\tau K_0(t-t') \frac{\partial \boldsymbol{\epsilon}^H}{\partial t'} dt', \tag{7}$$

where $\boldsymbol{\sigma}$ is the Cauchy stress, $\boldsymbol{\epsilon}^D$ and $\boldsymbol{\epsilon}^H$ are the deviatoric and hydrostatic portions of the Eulerian strain tensor. Here τ and t represent physical and reduced times. The bulk modulus K_0 of the polymer is assumed to be a constant, as in [41, 42]. The shear modulus G has a form of

$$G(t) = G_e + \sum_{i=1}^n G_i \exp\left(-\frac{t}{\tau_i^r}\right), \tag{8}$$

where G_e is the long term modulus when the binder is fully relaxed. Here, τ_i^r is the relaxation time of the i th mode, and G_i is the corresponding modulus, which is tabulated in Table 1.

In the present study, viscoplastic dissipation, viscoelastic dissipation, and heat conduction are the thermal–mechanical processes affecting the local temperature rise and consequent hotspot development in the PBX under dynamic loading.

Table 1 Parameters of Prony series for Estane binder in PBX 9501 from [41]

Frequency (Hz)	G_i (MPa)	Frequency (Hz)	G_i (MPa)
10^{-6}	0.00417	10^5	2.6182
10^{-5}	0.00741	10^6	12.882
10^{-4}	0.01585	10^7	52.481
10^{-3}	0.03802	10^8	223.87
10^{-2}	0.06761	10^9	436.52
10^{-1}	0.08913	10^{10}	457.09
1	0.1156	10^{11}	346.74
10^1	0.1422	10^{12}	251.19
10^2	0.1622	10^{13}	177.83
10^3	0.2218	10^{14}	117.49
10^4	0.4753	10^{15}	75.858

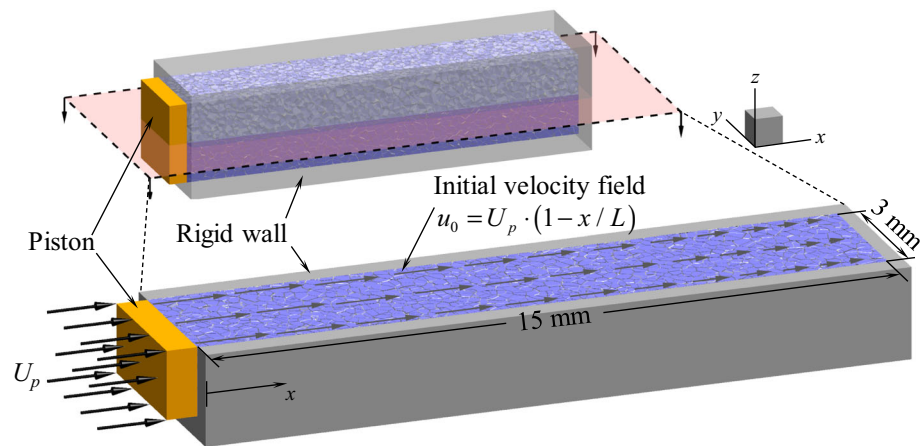
Further development can also include the effects of fracture, frictional contact, and frictional heating within the microstructure, as in previous 2D simulations [1, 18].

2.3 Lagrangian computational setup

The Lagrangian calculations are performed on the set of five statistically equivalent microstructure samples described in Sect. 2.1. The overall size is 15 mm × 3 mm × 3 mm. The objective is to characterize the heterogeneous heating resulting from microstructure processes and develop a means for capturing the mechanism that can be used as input data in the Eulerian calculations of the reaction and shock-to-detonation transition process. As illustrated in Fig. 4, the lateral (top, bottom, front, back) boundaries of the sample are confined such that displacement perpendicular to the surfaces are prevented. Impact loading is effected by applying a constant normal velocity U_p on the left (front) end of the sample. This configuration emulates the experimental condition of a piston impacting on a PBX specimen. To achieve overall consistent high-rate deformation throughout the sample, a linearly varying longitudinal velocity field is specified *initially and only initially* (at $t = 0$) along the sample length. Specifically, the magnitude of the initial axial velocity field has the form $u_0 = U_p \cdot (1 - x/L)$, where L is the sample length and x is the initial distance from the impact (left) end. The imposed particle velocity is in the range of $U_p = 200\text{--}2500$ m/s to cover a wide range of strain rate and stress levels typically seen in calculations and experiments [43–46]. Each sample is subject to loading in this range.

It is important to point out that this configuration does not exactly reproduce impact loading because of the imposition of the initial velocity field. This is intentional. Basically, this treatment creates the condition for subjecting a whole sample to overall macroscopically (not microstructurally)

Fig. 4 Configuration of the computational model for Lagrangian simulations with loading, boundary, and initial conditions shown on a cross section of the microstructure



uniaxial strain loading at different strain rates and load intensities, allowing the microstructure-sensitive heterogeneous deformation and heating to be analyzed and quantified. In particular, the objective here is to characterize the inelastic dissipation and heating in the microstructures and obtain a representation and, more importantly, a measure for the heterogeneous heating mechanism that can be used as input in the Eulerian simulations of the SDT process for the determination of the pop plot. The specific measure used here focuses on the net effects of all factors on heating and takes the form of the hotspot intensity field $\chi(x, y, z)$ which is defined as

$$\chi = \frac{T - T_{\text{ref}}}{T_{\text{max}} - T_{\text{ref}}}, \quad (9)$$

where T is temperature and T_{max} is the highest temperature in the microstructure under a given condition. T_{ref} is a reference temperature, which is taken as the initial temperature (300 K) of the material. The value of χ ranges from 0 to 1 and represents the relative strengths of heterogeneous heating in a microstructure that reflect the aggregate effects of microstructure, constituent behavior, deformation/dissipation mechanisms, and loading. As the results in Sect. 3 will show, this measure is largely invariant with respect to both time (or stages of deformation of a sample) and loading (strain rate and stress level as defined by the piston velocity U_p). This invariance suggests that χ can be used as a measure for the variations in heating or hotspot formation and potentially used in the homogenized model in the Eulerian simulations.

2.4 The Eulerian approach

2.4.1 Governing equations

The simulation of SDT in energetic materials such as PBX can be performed by solving the chemically reacting multiphysics Euler equations [47]. These equations correspond

to the conservation of mass, momentum, energy, and species mass in the form of

$$\begin{cases} \frac{\partial \rho}{\partial t} + \nabla \cdot (\rho \mathbf{u}) = 0, \\ \frac{\partial \rho \mathbf{u}}{\partial t} + \nabla \cdot (\rho \mathbf{u} \mathbf{u}) = -\nabla P, \\ \frac{\partial \rho E}{\partial t} + \nabla \cdot (\rho E + P) \mathbf{u} = 0, \text{ and} \\ \frac{\partial \rho \lambda}{\partial t} + \nabla \cdot (\rho \lambda) = -\dot{\omega}, \end{cases} \quad (10)$$

where ρ , \mathbf{u} , P , E , λ , and $\dot{\omega}$ denote mass density, velocity, pressure, total energy per unit mass, mass fraction reacted and the reaction rate, respectively. E is the sum of internal energy e and kinetic energy, i.e.,

$$E = e + \frac{\mathbf{u} \cdot \mathbf{u}}{2}. \quad (11)$$

The internal energy is defined as

$$e = c_v T + \lambda Q, \quad (12)$$

where Q is the heat release due to chemical reaction, T is temperature, and c_v is the specific heat per unit mass at constant volume. c_v is assumed to be constant and a simplified expression for the internal energy is used following past studies [6, 20, 47]. The modeling of the reaction rate $\dot{\omega}$ is based on a shock-pressure dependent Arrhenius-type rate model which has been used in past studies [48, 49] and is further discussed below in the chemistry modeling section.

2.4.2 Equations of state (EOS)

A hybridized version of the Mie–Grüneisen (MG) and Jones–Wilkins–Lee (JWL) equations of state (EOS) is used. Specifically, MG is used for the reactant and JWL is used for the product. Such an approach has been used in the past [50–52]. The MG EOS typically performs reasonably well for solid energetic materials [47, 53], however, its performance tends to deteriorate beyond the detonation wave front

Table 2 Material parameters in the MG and JWL equations of state for PBX

ρ_0 (kg/m ³)	Γ	s	c_0 (m/s)	c_v (J/kg-K)	e_0 (J/kg)
1732.8	0.76	1.772	2926	1701.6	5.1×10^5
A (GPa)	B (GPa)	E_0 (GPa)	R_1	R_2	ω
634.7	8.0	0.005	4.2	1.0	0.3

and the reaction zone, particularly, in the expanding gaseous products region where density attains lower values [53]. In such regions, the JWL EOS is known to perform better. The current hybridized approach is similar to that in past studies [50–52] and accounts for the effects of the EOS for both the reactants and the products. A brief description of the MG and the JWL equation of states and the hybridization procedure is given below.

The pressure from the MG EOS is

$$P^{MG} = \frac{\Gamma}{v} [e - e_0] + f(v), \tag{13}$$

where

$$\begin{cases} f(v) = P_H \left[1 - \frac{\Gamma}{2v} (v_0 - v) \right] - \frac{\Gamma}{2v} P_0 (v_0 - v), \\ P_H = P_0 + \frac{\rho_0 c_0 \eta}{(1-s\eta)^2}, \\ \eta = 1 - \frac{v_0}{v}, \text{ and} \\ v = 1/\rho. \end{cases} \tag{14}$$

In the above equations, v is the specific volume, P_H is the pressure along the Hugoniot, Γ is the Grüneisen gamma, s is the slope relating the shock speed and the particle velocity, and c_0 is the speed of sound. The pressure from the JWL EOS is

$$P = A \left(1 - \frac{\omega\rho}{R_1\rho_0} \right) e^{-\frac{R_1\rho_0}{\rho}} + B \left(1 - \frac{\omega\rho}{R_2\rho_0} \right) e^{-\frac{R_2\rho_0}{\rho}} + \omega\rho (c_v T - E_0), \tag{15}$$

where ρ_0 and E_0 are taken at the CJ point. The parameters corresponding to MG and JWL used are summarized in Table 2.

The hybridization of the MG and JWL equations of state is performed using a transition criterion based on the reactant mass fraction and the local density. Specifically, the mixture pressure in the simulations is given in terms of P^{MG} and P^{JWL} as

$$P = \begin{cases} P^{MG}, & \lambda > 0.01 \text{ or } \rho > 2500 \text{ kg/m}^3; \\ \lambda P^{MG} + (1 - \lambda) P^{JWL}, & 1000 \leq \rho \leq 2500 \text{ kg/m}^3; \\ P^{JWL}, & \rho < 1000 \text{ kg/m}^3. \end{cases} \tag{16}$$

The above empirical approach to hybridization allows for a smooth transition from the MG to the JWL equation of state. Other functional forms can also be utilized to ensure such a smooth transition. For the cases considered in the present study, this approach does not lead to any numerical instabilities, and therefore, can be considered adequate.

2.4.3 Chemistry model

The reaction-rate model for the PBX employs a pressure-dependent one-step Arrhenius formulation in the form of

$$\dot{\omega} = Af(P_s)\rho\lambda e^{-\frac{E_a}{RT}}, \tag{17}$$

where A is the pre-exponential factor, E_a is the activation energy, R is the gas constant, P_s is the shock pressure, and

$$f(P_s) = C \left(\frac{P_0}{P_s} \right)^n. \tag{18}$$

The values of A and E_a/R are $2.8 \times 10^{11} \text{ s}^{-1}$ and 17,900 K, respectively, following past studies [54, 55]. Parameters C , n , and P_0 are 60, 12.5 and 12.0 GPa, respectively, as obtained by calibrating to experimental run-up distance. Such models for the reaction rate have been used before, such as the DAGMAR (Direct Analysis Generated-Modified Arrhenius Rate) model [48, 49]. Typically, one-step Arrhenius reaction-rate models with temperature dependence only are suitable for SDT studies for the overall smaller sizes at the meso-scale level. For simulations at higher scales with run distances on the order of mm, typical of most experiments, pressure-dependent burn rates are required to produce experimentally measured pop plots [56]. Here, explicit dependence on pressure is introduced to the one-step Arrhenius model in a manner similar to that in the DAGMAR model. Such an approach essentially implies that the pre-exponential factor in the Arrhenius model depends upon the pressure. This has been reported previously [57].

2.4.4 Hotspot model

Explicit resolution of the microstructure and small-scale mechanisms in a 3D simulation tends to be computationally prohibitive. Here, a homogenized approach that allows the effects of microstructure and lower-scale mechanisms to be phenomenologically accounted for is developed. In this otherwise homogenized approach for simulating SDT,

a mechanistic hotspot model [8, 20] is used to imbue the effects of unresolved microstructure and small-scale phenomena through the hotspot intensity field discussed earlier. This approach allows the effects of heterogeneities and discontinuities such as constituent variations, interfaces, cracks and voids on the order of microns or sub-microns (which can cause ignition at much lower shock strengths [58]) to be phenomenologically accounted for. The mechanistic hotspot model used in this study is an extension of the model developed from the studies of void collapse. A brief discussion is given below. A complete description with underlying assumptions and applications can be found elsewhere [8, 20].

Hotspots are essentially local areas of higher temperatures where more intense heating occurs. What is considered “hot” is relative and primarily a reflection of the local intensity of heating. In the approach here, the internal energy is given by

$$e = c_v T + Q + \lambda_{\text{HS}} Q_{\text{HS}}, \quad (19)$$

where λ_{HS} denotes the mass fraction of the hotspot. The evolution of λ_{HS} is governed by the transport equation

$$\frac{\partial \rho \lambda_{\text{HS}}}{\partial t} + \nabla \cdot (\mathbf{u} \rho \lambda_{\text{HS}}) = -\dot{\omega}_{\text{HS}}. \quad (20)$$

Here, the reaction-rate is expressed as

$$\dot{\omega}_{\text{HS}} = \chi Z \rho \lambda_{\text{HS}} e^{-\frac{p_a}{p}}, \quad (21)$$

where $\chi(x, y, z)$ is the hotspot intensity field obtained from the Lagrangian meso-scale simulation, as defined in Eq. (9). Since the induction time for the energy deposition is specified via χ , higher values of χ give rise to faster energy deposition, reflecting the fact that stronger local dissipation leads to earlier onset of reaction. This approach is similar to but somewhat different from the original hotspot model described in [20], where an additional transport equation employing the induction parameter model [59] is solved to account for the effects of the induction time, which determines the duration between the passage of the shock at a hotspot location and when Q_{HS} is fully released. The modified hotspot model is complete after Q_{HS} and χ are specified. Based on the results of prior analyses, Q_{HS} is taken to be ~ 29 kJ/kg, or approximately 0.25% of Q . This value is lower than used in the hotspot model in past studies of void collapse [20], where Q_{HS} was about 7% of Q . This is reasonable as voids are not explicitly tracked here.

2.4.5 Numerical technique

A fully compressible finite volume multi-physics solver, referred to as LESLIE [60–62], is used. This is a well-established platform for shock and detonation studies. The

governing equations are spatially discretized using a third-order MUSCL (Monotonic Upwind Scheme for Conservation Laws) scheme and solved with the well-established HLLC (Harten, Lax, van Leer, and Einfeldt) approximate Riemann solver. The MUSCL scheme is well-known to yield accurate solutions for cases where shocks and discontinuities can be observed. The HLLC solver utilizes the integral form of the system of conservation laws and is a stable and robust approximate Riemann solver. The time integration of the spatially discretized equations is performed using a second-order-accurate predictor–corrector scheme.

2.5 Eulerian Computational Setup

The 3D SDT simulations are performed for a range of shock pressure (11–15 GPa) to obtain the pop plot. The computational domain is 15 mm \times 3 mm \times 3 mm in size and discretized into 750 \times 150 \times 150 uniform finite volume cells. Supersonic inflow/outflow boundary conditions are specified along the longitudinal (x) direction and a free-slip boundary condition is specified along the transverse (y or z) directions at the two ends of the domain. A schematic illustration of the computational setup with the initial hotspot field is shown in Fig. 5.

3 Results and discussion

In this section, the hotspot intensity fields are first obtained from the Lagrangian simulations using different samples. As mentioned before, these fields provide the coupling between the Lagrangian and the Eulerian models. The discussions focus on the SDT process in the Eulerian simulations. The pop plot obtained from the Eulerian simulations is compared with available experimental and computational data. An analytical expression for the material-dependent probabilistic SDT threshold is described.

3.1 Hotspot intensity field

Figure 6 shows the hotspot intensity fields for the five samples in Fig. 3 under a load intensity of 200 m/s. The hotspot intensity field for microstructure 1 is shown in Fig. 7a with the microstructure grain-binder profiles outlined. To reveal the interior of the field, a sectional view is used. There is a gravitation of the heating (higher values of the hotspot intensity) toward grain-binder boundaries, however, intense heating also occurs inside the grains. This observation in 3D is in consistent with what has been previously observed in 2D by Wei et al. [18]

The objective of the analysis here is to develop a measure for the spatial distribution of heterogeneous heating that reflects the effects of microstructure on heating. Therefore,

Fig. 5 Schematic illustration of the 3D computational setup for the Eulerian calculations

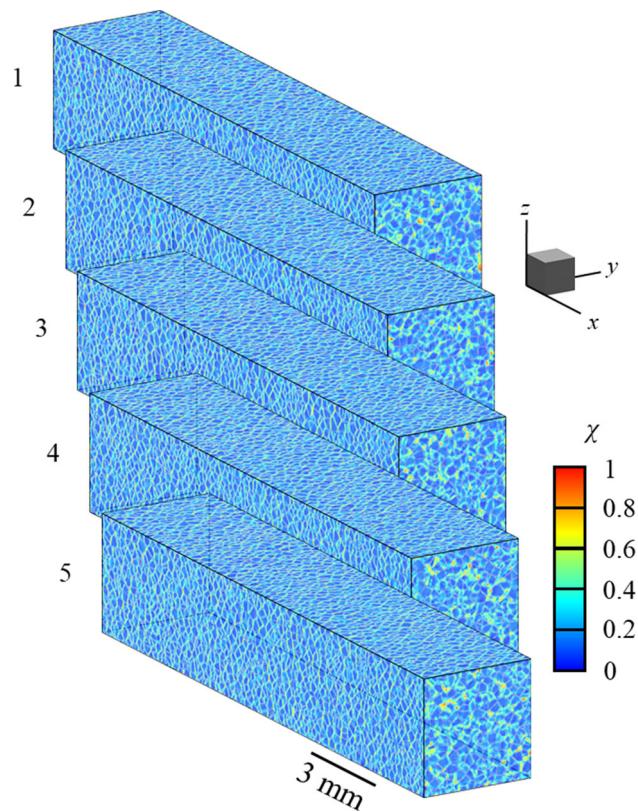
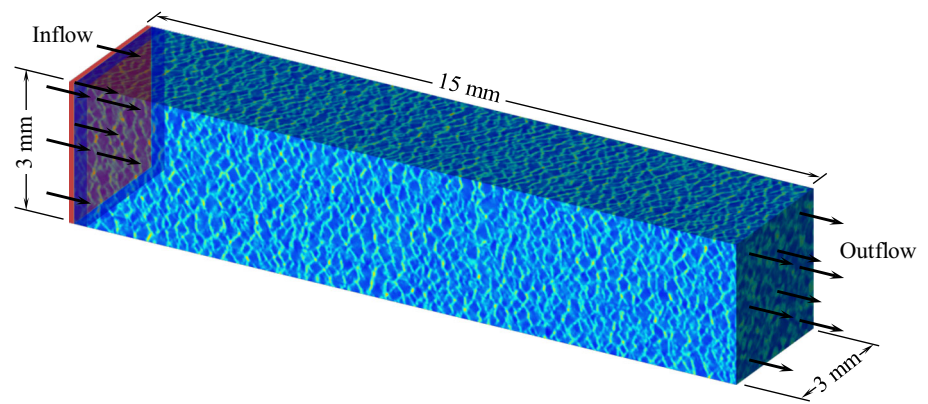


Fig. 6 Hotspot intensity field for all the five samples

the characteristics of the hotspot intensity field in different stages of deformation and at different load intensities are of interest. For comparison, the distributions of $\chi(x, y, z)$ on the random cross-section at $x_{init} = 4.025$ mm at three different times ($t = 20, 25,$ and $30 \mu\text{s}$) for $U_p = 200$ m/s are shown in Fig. 7b–d. The corresponding overall axial strain is 27%, 33%, and 40%. Clearly, the fields are quite similar to each other in terms of spatial location, variation, and intensity, indicating that χ remains nearly constant over different stages of deformation. Similarly, the distributions of χ for different load intensities at $U_p = 200, 600,$ and 1000 m/s at $t = 25, 8,$ and $5 \mu\text{s}$ respectively (corresponding overall axial strain is 33%) are shown in Fig. 7c, e, f.

Again, the fields are quite similar to each other, with only slight increase in the intensity at the higher load levels (Fig. 7g). The root-mean-square difference among all these cases is within 17% of the mean. These results show that the hotspot intensity field χ is largely consistent under different conditions throughout the deformation. Since the field is dependent on microstructures but is largely invariant with respect to loading and stage of deformation, it can be used as a surrogate for microstructure to approximate the aggregate effects of material heterogeneities on heating. Such heating is the mechanism leading to the initiation of chemical reaction even in an otherwise homogenized setting. In this study, this surrogate is used in the Eulerian model for reaction initiation, reaction propagation, and SDT.

3.2 SDT Process

Figure 8 shows the distributions of pressure in a sample at three different times in the SDT process. The load intensity is $P_s = 11$ GPa. The passage of the shock wave imparts energy into the material and causes temperature to increase. Ignition is observed locally at around 368 ns (Fig. 8a), with the reaction front exhibiting a non-uniform and complex structure in 3D. The ignition occurs at multiple locations, followed by growth and coalescence. This process leads to the formation of a detonation front which initially has a complex shape but rapidly becomes planar (Fig. 8b, c). The planar detonation front propagates faster than the shock front ahead and eventually catches up to the shock front at approximately 495 ns (Fig. 8c), thereby completing the SDT process. The distance between the initial impact face and the location of the detonation and shock fronts at the moment of SDT completion (Fig. 8c) is the run-to-detonation distance or the run distance x^* , which is used as a measure for the macroscopic performance of an energetic material. Since this performance measure depends on the load intensity P_s , the relationship between x^* and P_s on a logarithmic scale in graphical form is called the pop plot [44], which will be further discussed in the next subsection.

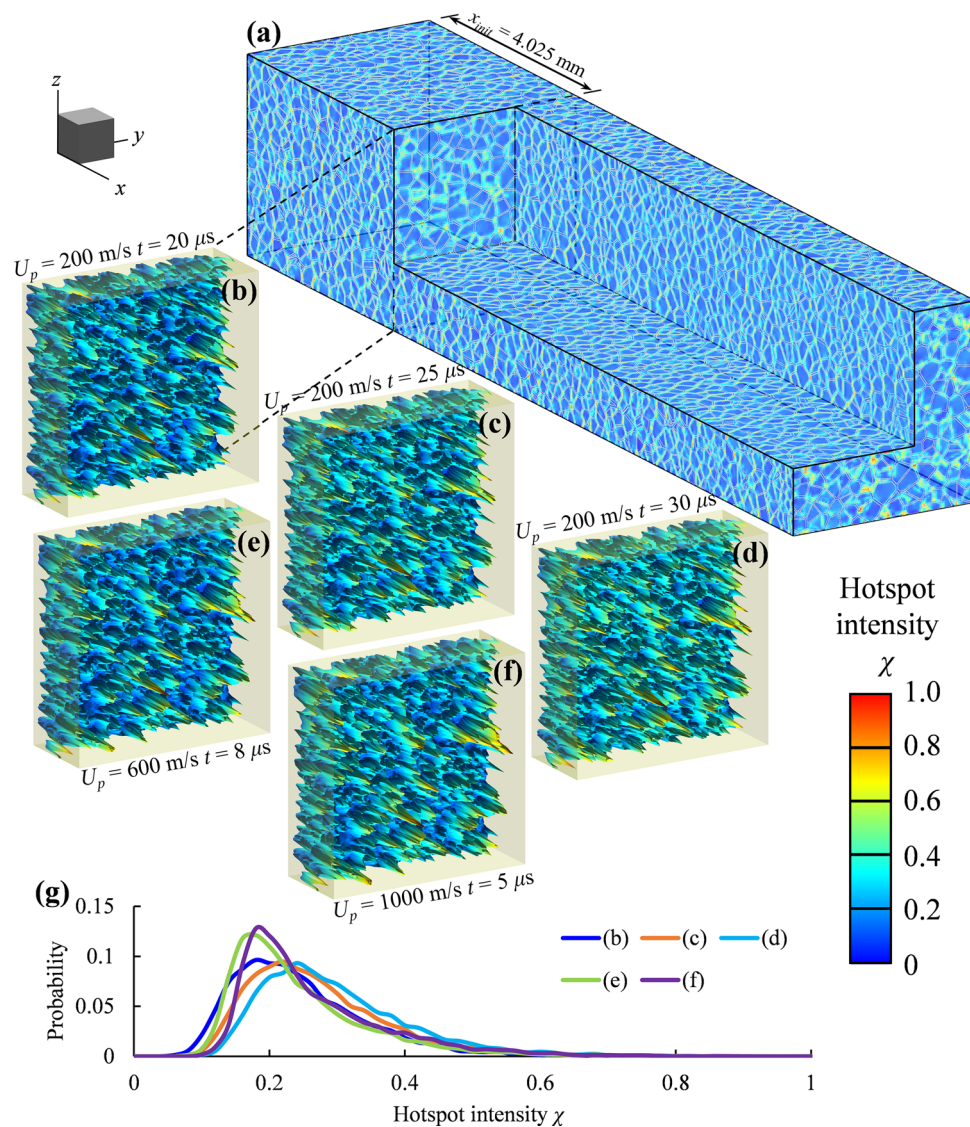


Fig. 7 Hotspot locations **a** in the whole sample and at the cross section of $x_{init} = 4.025 \text{ mm}$ when **b** $U_p = 200 \text{ m/s}$, and $t = 20 \mu\text{s}$, **c** $U_p = 200 \text{ m/s}$, and $t = 25 \mu\text{s}$, **d** $U_p = 200 \text{ m/s}$, and $t = 30 \mu\text{s}$,

e $U_p = 600 \text{ m/s}$, and $t = 8 \mu\text{s}$, **f** $U_p = 1000 \text{ m/s}$, and $t = 5 \mu\text{s}$, and **g** probability distributions of hotspot intensity fields in **(b)**, **(c)**, **(d)**, **(e)**, and **(f)**

The results show that the 3D model based on the heating intensity from the Lagrangian calculations can capture the overall heterogeneous nature of the reaction and SDT process of a PBX. To illustrate the statistical variations of the behavior along different samples, the distributions of pressure for five samples are shown in Fig. 9 for $t = 398 \text{ ns}$. Clearly, there are significant variations among the samples. It is the variations and the resulting difference in the run distance x^* under the same loading that allow the statistical behavior, in particular, the statistical scatter in the pop plot, to be quantified.

3.3 Pop plot

Figure 10 shows the pop plot obtained from the 3D simulations using multiple samples over a range of load intensity. Specifically, the five samples are used at each shock intensity as measured by the input pressure (shock pressure). The mean, maximum and minimum run-up distances for each shock pressure are shown by the blue symbols and the error bars. The uncertainties in the determination of the run distance are found to be small ($\sim 4\text{--}5\%$) due to the well-defined nature of the planar detonation front at the run distance or completion of SDT (Fig. 8). Overall, the calculated SDT

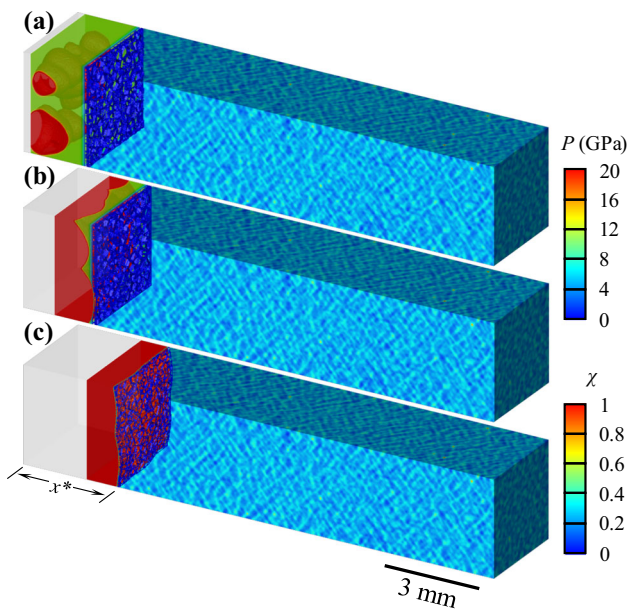


Fig. 8 The SDT process of a sample for $P_s = 11$ GPa, **a** at ignition, **b** detonation front homogenization and growth behind the shock front, and **c** at run-up distance. The corresponding times are 368 ns, 398 ns, and 495 ns, respectively

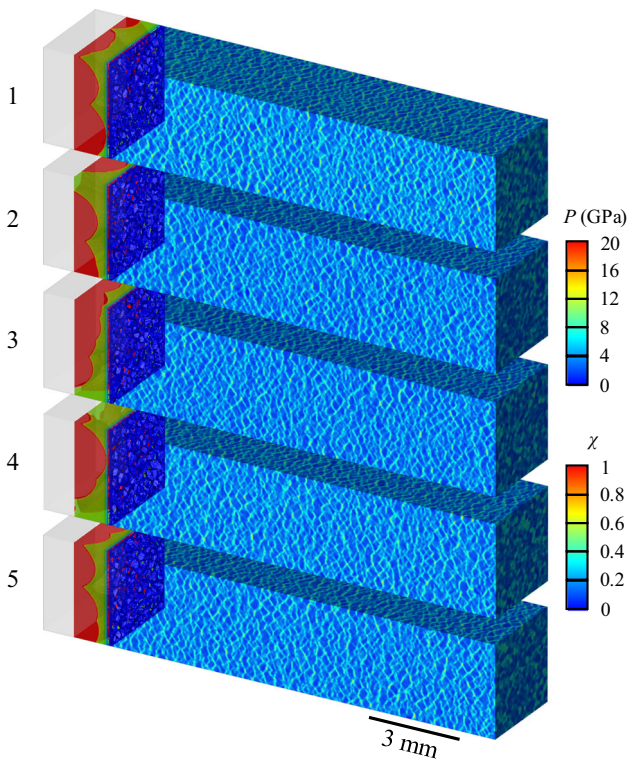


Fig. 9 Distributions of pressure in five samples at $t = 398$ ns for $P_s = 11$ GPa

threshold here is in good agreement with the experimentally and computationally obtained pop plots [43–45, 63] in the literature.

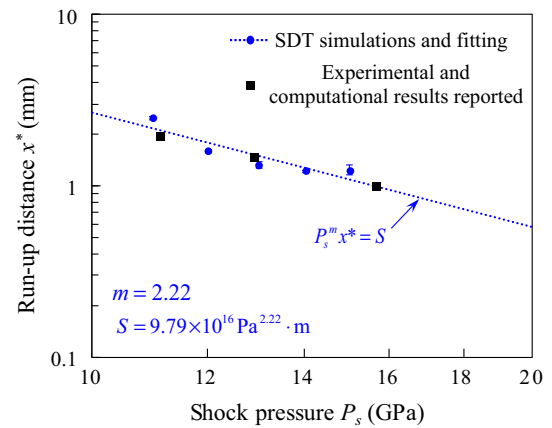


Fig. 10 Pop plot obtained from calculations over a range of shock pressure. The blue circular symbols denote the mean run-up distances among the five samples for each pressure. The error bars denote range of variation among the five samples in the SEMSS. The blue dotted line denotes fit of the mean to Eq. (22). The black square symbols represent data points reported in the literature [43–45, 63]. (Color figure online)

3.4 Analytical form for pop plot and probability of SDT

The linear relationship between P_s and x^* in pop plots like Fig. 10 in logarithmic scales can be represented by

$$\frac{P_s^m x^*}{S} = 1, \tag{22}$$

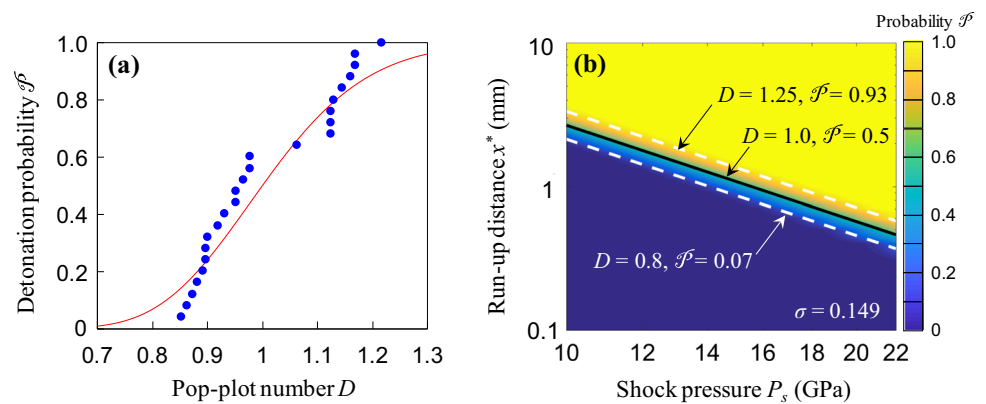
where x^* is the run distance to detonation, and S and m are parameters that are dependent on material and microstructure. This relation can be used to relate the mean run distance and the shock pressure. To account for the probabilistic nature of detonation in the $P_s - x^*$ space, we introduce another parameter D which we call the pop plot number such that the above relation is modified to

$$\frac{P_s^m x^*}{S} = D. \tag{23}$$

Here $D = 1$ corresponds to the mean pop plot relation in Eq. (22) with a 50% probability of detonation for a given shock pressure and run distance pair, $D > 1$ (shifting the line upward) corresponds to load and distance conditions for SDT probabilities greater than 50%, and $D < 1$ (shifting the line downward) corresponds to conditions for SDT probabilities less than 50%. Obviously, D quantifies the likelihood of SDT.

Under the assumption that the scatter of data points (and, therefore, the probability distribution) about the threshold line at $D = 1$ is symmetric in Fig. 10 (log–log scale) and can be described by the normal distribution, it has been shown

Fig. 11 **a** SDT probability as a function of the pop plot number D , the red solid line indicates fit of the blue data points to Eq. (24), and **b** SDT probability map in the $P_s - x^*$ space, as obtained from the simulation results



[1] that the specific form for the probability of detonation under such conditions is

$$\mathcal{P}(D) = \frac{1}{\sigma\sqrt{2\pi}} \int_{-\infty}^D \frac{1}{x} \exp\left[-\frac{(\ln x)^2}{2\sigma^2}\right] dx = \frac{1}{2} \left[1 + \operatorname{erf}\left(\frac{\ln D}{\sqrt{2}\sigma}\right) \right], \quad (24)$$

where σ is the standard deviation which is obtained by fitting all the data points in Fig. 11a to Eq. (24). These data points concern all the samples in the SEMSS for all shock pressures analyzed in aggregate. Combining Eqs. (23) and (24) yields a direct relation between the SDT probability \mathcal{P} and the loading condition parameter P_s and the run distance x^* in the form of

$$\mathcal{P}(P_s, x^*) = \frac{1}{2} + \frac{1}{2} \operatorname{erf}\left[\frac{1}{\sqrt{2}\sigma} (\ln(P_s^m x^*) - \ln S) \right]. \quad (25)$$

This relation allows the material-dependent SDT probability map in Fig. 11b to be generated. The relation and the map enable the prediction of SDT probability for any combination P_s and x^* and the establishment of the SDT threshold (P_s, x^*) corresponding to any given level of probability.

4 Conclusions and comments

The establishment of macroscopic engineering measures of material performance as functions of microstructure is a fundamental challenge in material science and mechanics. The task requires explicit resolution of microstructure, account of relevant physical processes, and quantification of the stochastic variations in material behaviors arising from intrinsic microscopic heterogeneities. As a measure for the performance of energetic materials, the pop plot (PP) or the relation between shock pressure and run distance to detonation is intrinsically dependent on the microstructure of the materials. The prediction of the relation requires tracking of coupled mechanical-thermal-chemical and trans-

port processes as well as microstructure. The task requires capabilities that are not readily available in one single computational approach.

In this paper, a computational framework integrating simulations based on a 3D Lagrangian computational framework (CODEX) and simulations based on an Eulerian computational framework (LESLIE) is developed. The aim is to predict the pop plot for a class of energetic materials known as PBXs with account of the underlying multiphysics processes and the effects of microstructure. While the Lagrangian part focuses on the thermal-mechanical processes, explicit resolution of microstructure, and deformation and heating leading to development of hotspots, the Eulerian part focuses on tracking the initiation/propagation of reaction, shock-to-detonation transition (SDT), and calculation of the pop plot. The two parts are linked through data transfer in the form of a hotspot intensity field or heating intensity field (HIF). This is made possible and justified by the observation that the scaled temperature field leading up to initiation of reaction (referred to as the hotspot intensity field or the heating intensity field) is largely invariant with respect to the stages of deformation and load intensity. The implication of this fact is that the heating characteristics of a PBX reflect the aggregate microstructure, material, and loading effects and therefore can be used as a surrogate for explicitly resolved microstructures in the Eulerian simulations of the reaction and SDT process. In the framework developed here, the HIF affects the reaction rate as the onset and progression of reaction depend on the heating rate due to thermal-mechanical dissipation under loading. Since this is a first attempt in such a framework, it is arguable as to if this treatment may be overly simplified or if better treatments can be found. Further exploration is certainly warranted. Future developments can include, for example, explicit resolution of voids, cracks, and crack-face friction.

This framework is used to obtain the pop plot of a PBX that echoes the microstructure and constituent attributes of PBX 9501. The calculated results are in agreement with the experimental and computational results reported in the liter-

ature. A set of statistically equivalent microstructure sample set (SEMSS) is generated and used in the simulations. The method is the computational equivalent of using multiple specimens in experiments to establish the statistical distribution of measured material properties. The use of the SEMSS over a range of loading conditions not only establishes a means for quantifying the statistical variations in the SDT behavior (pop plot) of the material analyzed, but also lead to the development of a probabilistic formula ($P_s^m x^*/S = D$) for predicting (1) the probability of detonation completion at any given combination of shock pressure and run distance, and (2) the threshold relation between shock pressure and run distance for any level of SDT probability. Although the results in this paper concern only a specific material system (PBX) and one material setting (volume fraction), ultimately, future analyses for other materials, microstructures, and constituent settings can allow the parameters in the analytical formula developed to be established as functions of microstructure and material properties. Such functions can then be used to characterize and analyze the behaviors of different materials. Further, trends and mechanisms can be identified to provide guidance for the synthesis of new materials with desired attributes not yet available, which is a task of material design. It is also useful to note that the SEMSS-based simulations can generate large numbers of datasets with the intertwining effects of many different factors which can be interdependent. As such, neural network (NN) based machining learning (ML) tools and methods [64, 65] can play an important role in delineating and quantifying the relations and influences embodied in the datasets. Furthermore, the framework naturally lends itself to uncertainty quantification (UQ) [24–30]. This is an emerging area that is worth exploring in the near future.

It is helpful to put the current approach in perspective. First, the domain size in the Lagrangian and Eulerian calculations are identical. As such, the approach can be regarded as only a homogenization step in connecting the microstructure scale and the macroscopic response scale. This is made possible by the fact that the sample size is in the mm scale which is greater than the range of run distances studied and much larger than the characteristic size scale of the microstructure. If issues involving larger sizes (e.g., hundreds or thousands of mm) are to be analyzed, an upscaling step is necessary and can be undertaken to avoid the 3D calculations to be prohibitively expensive. Such a step is not attempted here and remains to be pursued in the future. Second, the chemical kinetics model used here is homogenized and requires independent calibration for the specific material composition or constituent volume fractions. This can be regarded as a limitation. To consider other compositions or constituent volume fraction levels, separate calibration will be required. It remains to be seen how this limitation can be alleviated.

Further development is desired for this new approach which is still in its early form.

Finally, we note that although PBXs with coupled mechanical-thermal-chemical-transport processes are the material system of focus here, the approach proposed can be used for materials with other underlying physical or multi-physical processes. Examples include materials whose combined thermal, mechanical, chemical, and piezo-electrical properties are of interest.

Acknowledgements Funding from the Defense Threat Reduction Agency (Dr. Douglas Allen Dalton) under HDTRA1-18-1-0004 (YW, UR, JHS, and MZ) and the Office of Naval Research (Dr. Chad Stoltz) under N00014-16-1-2060 (RR and SM) is gratefully acknowledged. Some of the calculations are performed on supercomputers at the AFRL, ARL, Navy and ERDC DSRCs of the U.S. DoD High Performance Computing Modernization Program.

References

- Kim S, Wei Y, Horie Y, Zhou M (2018) Prediction of shock initiation thresholds and ignition probability of polymer-bonded explosives using mesoscale simulations. *J Mech Phys Solids* 114:97–116. <https://doi.org/10.1016/j.jmps.2018.02.010>
- Long Y, Chen J (2015) Systematic study of the reaction kinetics for HMX. *J Phys Chem A* 119(18):4073–4082. <https://doi.org/10.1021/jp509144v>
- Yarrington CD, Wixom RR, Damm DL (2018) Shock interactions with heterogeneous energetic materials. *J Appl Phys* 123(10):105901. <https://doi.org/10.1063/1.5022042>
- Tran L, Udaykumar HS (2006) Simulation of void collapse in an energetic material. Part 2: Reactive case. *J Propul Power* 22(5):959–974. <https://doi.org/10.2514/1.13147>
- Austin RA, Barton NR, Howard WM, Fried LE (2014) Modeling pore collapse and chemical reactions in shock-loaded HMX crystals. *J Phys: Conf Ser* 500(5):052002. <https://doi.org/10.1088/1742-6596/500/5/052002>
- Jackson TL, Buckmaster JD, Zhang J, Anderson MJ (2015) Pore collapse in an energetic material from the micro-scale to the macro-scale. *Combust Theor Model* 19(3):347–381. <https://doi.org/10.1080/13647830.2015.1026401>
- Barua A, Kim S, Horie Y, Zhou M (2013) Prediction of probabilistic ignition behavior of polymer-bonded explosives from microstructural stochasticity. *J Appl Phys* 113(18):184907. <https://doi.org/10.1063/1.4804251>
- Akiki M, Gallagher TP, Menon S (2017) Mechanistic approach for simulating hot-spot formations and detonation in polymer-bonded explosives. *AIAA J* 55(2):585–598. <https://doi.org/10.2514/1.J054898>
- Souers PC, Forbes JW, Fried LE, Howard WM, Anderson S, Dawson S, Vitello P, Garza R (2001) Detonation energies from the cylinder test and CHEETAH V3.0. *Propell Explos Pyrot* 26(4):180–190. [https://doi.org/10.1002/1521-4087\(200110\)26:4<180::AIDPREP180>3.0.CO;2-K](https://doi.org/10.1002/1521-4087(200110)26:4<180::AIDPREP180>3.0.CO;2-K)
- Kuo I, Bastea S, Fried L (2010) Reactive flow modeling of liquid explosives via ALE3D/Cheetah simulations. In: 14th international detonation symposium, Coeur d'Alene, ID, United States, 2010
- Handley C, Whitworth N, James H, Lambourn B, Maheswaran MA (2010) The CREST reactive-burn model for explosives. In: EPJ web conferences, vol 10. <https://doi.org/10.1051/epjconf/20101000004>

12. Shukla RK, Pantano C, Freund JB (2010) An interface capturing method for the simulation of multi-phase compressible flows. *J Comput Phys* 229(19):7411–7439. <https://doi.org/10.1016/j.jcp.2010.06.025>
13. Rai NK, Udaykumar HS (2018) Three-dimensional simulations of void collapse in energetic materials. *Phys Rev Fluids* 3(3):033201. <https://doi.org/10.1103/physrevfluids.3.033201>
14. Skidmore C, Phillips D, Howe P, Mang J, Romero J (1998) The evolution of microstructural changes in pressed HMX explosives. In: 11th symposium (international) on detonation, Snowmass Village, CO, 1998
15. Skidmore CB, Phillips DS, Son SF, Asay BW (1998) Characterization of HMX particles in PBX 9501. *AIP Conf Proc* 429(1):579–582. <https://doi.org/10.1063/1.55666>
16. Baer MR (2002) Modeling heterogeneous energetic materials at the mesoscale. *Thermochim Acta* 384(1–2):351–367. [https://doi.org/10.1016/S0040-6031\(01\)00794-8](https://doi.org/10.1016/S0040-6031(01)00794-8)
17. Baer MR, Gartling DK, DesJardin PE (2012) Probabilistic models for reactive behaviour in heterogeneous condensed phase media. *Combust Theor Model* 16(1):75–106. <https://doi.org/10.1080/13647830.2011.606916>
18. Wei Y, Kim S, Horie Y, Zhou M (2018) Quantification of probabilistic ignition thresholds of polymer-bonded explosives with microstructure defects. *J Appl Phys* 124(16):165110. <https://doi.org/10.1063/1.5031845>
19. Noble CR, Anderson AT, Barton NR, Bramwell JA, Capps A, Chang MH, Chou JJ, Dawson DM, Diana ER, Dunn TA (2017) Ale3d: an arbitrary Lagrangian-Eulerian multi-physics code. Lawrence Livermore National Lab (LLNL), Livermore
20. Akiki M, Menon S (2015) A model for hot spot formation in shocked energetic materials. *Combust Flame* 162(5):1759–1771. <https://doi.org/10.1016/j.combustflame.2014.11.037>
21. Najjar FM, Howard WM, Fried LE, Manaa MR, Nichols A, Levesque G (2012) Computational study of 3-D hot-spot initiation in shocked insensitive high-explosive. In: AIP conference proceedings, vol 1426. <https://doi.org/10.1063/1.3686267>
22. Nichols AL, Tarver CM, McGuiire EM (2004) ALE3D statistical hot spot model results for LX-17. Shock compression of condensed matter - 2003, Pts 1 and 2, Proceedings 706:397–400
23. Austin RA, Barton NR, Reaugh JE, Fried LE (2015) Direct numerical simulation of shear localization and decomposition reactions in shock-loaded HMX crystal. *J Appl Phys* 117(18):185902. <https://doi.org/10.1063/1.4918538>
24. Akiki M, Gallagher T, Hannebique G, Menon S (2017) Uncertainty quantification in the simulation of explosive particle dispersal using an Eulerian/Lagrangian formulation. In: 55th AIAA aerospace sciences meeting, 2017, p 0600
25. Schulz JC, Gottiparthi KC, Menon S (2015) Uncertainty quantification of bacterial aerosol neutralization in shock heated gases. *Shock Waves* 25(1):77–90. <https://doi.org/10.1007/s00193-014-0545-0>
26. Zhang D, Lu L, Guo L, Karniadakis GE (2018) Quantifying total uncertainty in physics-informed neural networks for solving forward and inverse stochastic problems. *arXiv preprint arXiv:180908327*
27. Lin G, Su CH, Karniadakis GE (2006) Predicting shock dynamics in the presence of uncertainties. *J Comput Phys* 217(1):260–276. <https://doi.org/10.1016/j.jcp.2006.02.009>
28. Xiu DB, Karniadakis GE (2002) Modeling uncertainty in steady state diffusion problems via generalized polynomial chaos. *Comput Methods Appl Mech Eng* 191(43):4927–4948. [https://doi.org/10.1016/S0045-7825\(02\)00421-8](https://doi.org/10.1016/S0045-7825(02)00421-8)
29. Xiu DB, Karniadakis GE (2003) Modeling uncertainty in flow simulations via generalized polynomial chaos. *J Comput Phys* 187(1):137–167. [https://doi.org/10.1016/S0021-9991\(03\)00092-5](https://doi.org/10.1016/S0021-9991(03)00092-5)
30. Xiu DB, Karniadakis GE (2003) A new stochastic approach to transient heat conduction modeling with uncertainty. *Int J Heat Mass Transf* 46(24):4681–4693. [https://doi.org/10.1016/S0017-9310\(03\)00299-0](https://doi.org/10.1016/S0017-9310(03)00299-0)
31. Christiansen DE, Taylor JW (1973) HE Sensitivity Study. Los Alamos Scientific Lab, Los Alamos
32. Hayes DB (1976) A Pnt detonation criterion from thermal explosion theory. In: 6th international detonation symposium, Coronado, CA, pp 95–100
33. Bennett JG, Haberman KS, Johnson JN, Asay BW (1998) A constitutive model for the non-shock ignition and mechanical response of high explosives. *J Mech Phys Solids* 46(12):2303–2322. [https://doi.org/10.1016/S0022-5096\(98\)00011-8](https://doi.org/10.1016/S0022-5096(98)00011-8)
34. Benson DJ, Conley P (1999) Eulerian finite-element simulations of experimentally acquired HMX microstructures. *Modell Simul Mater Sci Eng* 7(3):333–354. <https://doi.org/10.1088/0965-0393/7/3/304>
35. Mas EM, Clements BE, Ionita A, Peterson P (2006) Finite element method calculations on statistically consistent microstructures of PBX 9501. *AIP Conf Proc* 845(1):487–490. <https://doi.org/10.1063/1.2263366>
36. Barua A, Zhou M (2011) A Lagrangian framework for analyzing microstructural level response of polymer-bonded explosives. *Model Simul Mater Sci Eng* 19(5):055001. <https://doi.org/10.1088/0965-0393/19/5/055001>
37. Dattelbaum DM, Stevens LL (2008) Chap 4. Equations of state of binders and related polymers. In: Peiris SM, Piermarini GJ (eds) Static compression of energetic materials. Shock wave and high pressure phenomena. Springer, Virginia, pp 127–202
38. Liu C (2003) Specific surface: a missing parameter in high-explosive modeling. Los Alamos National Laboratory (LANL), Los Alamos
39. Zhang R, Zhang MP, Shu CW (2011) On the order of accuracy and numerical performance of two classes of finite volume WENO schemes. *Commun Comput Phys* 9(3):807–827. <https://doi.org/10.4208/cicp.291109.080410s>
40. Zhou M, Needleman A, Clifton RJ (1994) Finite-element simulations of shear localization in plate impact. *J Mech Phys Solids* 42(3):423–458. [https://doi.org/10.1016/0022-5096\(94\)90026-4](https://doi.org/10.1016/0022-5096(94)90026-4)
41. Mas EM, Clements BE, Blumenthal B, Cady CM, Gray GT, Liu C (2002) A viscoelastic model for PBX binders. *AIP Conf Proc* 620:661–664. <https://doi.org/10.1063/1.1483625>
42. Wu Y-Q, Huang F-L (2009) A micromechanical model for predicting combined damage of particles and interface debonding in PBX explosives. *Mech Mater* 41(1):27–47. <https://doi.org/10.1016/j.mechmat.2008.07.005>
43. Peterson JR, Wight CA (2012) An Eulerian-Lagrangian computational model for deflagration and detonation of high explosives. *Combust Flame* 159(7):2491–2499. <https://doi.org/10.1016/j.combustflame.2012.02.006>
44. Gibbs TR, Popolato A (1980) LASL explosive property data. University of California, Berkeley
45. Vandersall KS, Tarver CM, Garcia F, Chidester SK (2010) On the low pressure shock initiation of octahydro-1,3,5,7-tetranitro-1,3,5,7-tetrazocine based plastic bonded explosives. *J Appl Phys* 107(9):094906. <https://doi.org/10.1063/1.3407570>
46. Gustavsen R, Sheffield S, Alcon R, Hill L (2002) Shock initiation of new and aged PBX 9501. In: Proceedings of the 12th international detonation symposium, San Diego, CA, USA, 2002. Citeseer, pp 530–537
47. Zhang J, Jackson TL, Buckmaster JD, Freund JB (2012) Numerical modeling of shock-to-detonation transition in energetic materials. *Combust Flame* 159(4):1769–1778. <https://doi.org/10.1016/j.combustflame.2011.11.010>
48. Wackerle J, Rabie R, Ginsberg M, Anderson A (1978) Proceedings of the symposium on high dynamic pressures. Commissariat a l’Energie Atomique Paris France

49. Anderson A, Ginsberg M, Seitz W, Wackerle J (1981) Seventh symposium (international) on detonation. Naval Surface Weapons Center NSWC MP82-334, p 385
50. Kim B, Jang SG, Yoh JJ (2017) A full-scale hydrodynamic simulation of energetic component system. *Comput Fluids* 156:368–383. <https://doi.org/10.1016/j.compfluid.2017.08.010>
51. Kim B, Kim M, Yoh JJ (2017) Shock to detonation transition analysis using experiments and models. *Proc Combust Inst* 36(2):2699–2707. <https://doi.org/10.1016/j.proci.2016.08.080>
52. Whitley VH, Stalsberg KL, Reichelt BL, Shipley SJ (2018) Model comparisons of the reactive burn model SURF in three ASC codes. Los Alamos National Lab (LANL), Los Alamos
53. Arienti M, Morano E, Shepherd J (2004) Shock and detonation modeling with the Mie–Grüneisen equation of state
54. Henson BF, Asay BW, Smilowitz LB, Dickson PM (2002) Ignition chemistry in HMX from thermal explosion to detonation. Shock compression of condensed matter-2001, Pts 1 and 2, Proceedings 620:1069–1072
55. Menikoff R (2006) Detonation waves in PBX 9501. *Combust Theor Model* 10(6):1003–1021. <https://doi.org/10.1080/13647830600851754>
56. Menikoff R (2008) Comparison of constitutive models for plastic-bonded explosives. *Combust Theor Model* 12(1):73–91. <https://doi.org/10.1080/13647830701414254>
57. Glascoe EA, Zaug JM, Burnham AK (2009) Pressure-dependent decomposition kinetics of the energetic material HMX up to 3.6 GPa. *J Phys Chem A* 113(48):13548–13555. <https://doi.org/10.1021/jp905276k>
58. Tarver CM, Chidester SK, Nichols AL (1996) Critical conditions for impact- and shock-induced hot spots in solid explosives. *J Phys Chem* 100(14):5794–5799. <https://doi.org/10.1021/jp953123s>
59. Sichel M, Tonello NA, Oran ES, Jones DA (2002) A two-step kinetics model for numerical simulation of explosions and detonations in H-2-O-2 mixtures. *Proc R Soc A Math Phys* 458(2017):49–82. <https://doi.org/10.1098/rspa.2001.0853>
60. Genin F, Menon S (2010) Dynamics of sonic jet injection into supersonic crossflow. *J Turbul* 11(4):1–30. <https://doi.org/10.1080/14685240903217813>
61. Genin F, Menon S (2010) Studies of shock/turbulent shear layer interaction using large-eddy simulation. *Comput Fluids* 39(5):800–819. <https://doi.org/10.1016/j.compfluid.2009.12.008>
62. Schulz JC, Gottiparthi KC, Menon S (2012) Ionization in gaseous detonation waves. *Shock Waves* 22(6):579–590. <https://doi.org/10.1007/s00193-012-0412-9>
63. Chidester SK, Thompson DG, Vandersall KS, Idar DJ, Tarver CM, Garcia F, Urtiew PA (2007) Shock initiation experiments on PBX 9501 explosive at pressures below 3 GPa with associated ignition and growth modeling. *AIP Conf Proc* 955(1):903–906. <https://doi.org/10.1063/1.2833274>
64. Pang G, Yang L, Karniadakis GE (2018) Neural-net-induced Gaussian process regression for function approximation and PDE solution. arXiv preprint [arXiv:1806.11187](https://arxiv.org/abs/1806.11187)
65. Goodfellow I, Pouget-Abadie J, Mirza M, Xu B, Warde-Farley D, Ozair S, Courville A, Bengio Y (2014) Generative adversarial nets. In: *Advances in neural information processing systems*, 2014, pp 2672–2680

Publisher's Note Springer Nature remains neutral with regard to jurisdictional claims in published maps and institutional affiliations.